A&A 398, 937–948 (2003)
DOI: 10.1051/0004-6361:20021710

Astronomy & Astrophysics

The polarized disk in M 31 at λ6 cm

E. M. Berkhuijsen, R. Beck, and P. Hoernes

Max-Planck-Institut für Radioastronomie, Auf dem Hügel 69, 53121 Bonn, Germany

Received 8 August 2002 / Accepted 7 November 2002

Abstract. We present a radio continuum survey of M 31 at λ6.2 cm with high sensitivity in total power and polarization, observed with the 100-m Effelsberg dish with an angular resolution of 2.′4. **(1)** Combination with the VLA + Effelsberg map at λ20.5 cm in total power yielded a spectral index map at 3′ resolution. Both the spectrum of the integrated emission and the spectral index distribution across M 31 indicate a nonthermal spectral index $\alpha_{\rm n} = 1.0 \pm 0.2$. We derived maps of thermal and nonthermal emission at λ6.2 cm. Radial profiles of the various emission components north and south of the minor axis revealed that the stronger total emission in the northern part of M 31 is entirely due to stronger thermal emission, whereas the profiles of nonthermal and polarized emission are nearly identical on either side of the minor axis. This suggests that recent star formation does not lead to a local increase of the number of relativistic electrons and/or magnetic field strength. **(2)** We discuss several properties of the polarized emission from M 31 and their implications for the magnetic field. At λ6.2 cm the polarized intensity systematically varies along the bright "ring" of emission which shows that the regular magnetic field, $B_{\rm reg}$, is nearly aligned with the spiral arms forming this "ring". The variation of the rotation measures between λ11.1 cm and λ6.2 cm, $RM(11, 6)$, across the galaxy confirms this alignment. The nonthermal degree of polarization reaches values >50% near the polarization maxima, implying that the *magnetic field in M 31 is exceptionally regular.* **(3)** We derived the distribution of the nonthermal depolarization between λ11.1 cm and λ6.2 cm, $DP_{\rm n}(11, 6)$, which is a measure of Faraday depolarization. Gradients in $RM(11, 6)$ may be an important cause of Faraday depolarization in M 31. The lack of anticorrelation between the thermal emission, which comes mainly from dense H II regions with small filling factors, and $RM(11, 6)$ and $DP_{\rm n}(11, 6)$ indicates that *rotation measures and Faraday depolarization originate in the extended diffuse ionized gas.*

Key words. galaxies: individual: M 31 – galaxies: spiral – galaxies: magnetic fields – ISM: magnetic fields – radio continuum: galaxies – polarization

1. Introduction

The Andromeda galaxy, M 31, is one of the best studied spirals of the Local Group. Its proximity (690 kpc, G. and A. de Vaucouleurs 1964[1]) and large angular extent on the sky (>3° along the major axis) enable observations with high linear resolution (≲100 pc), even at radio wavelengths, allowing detailed studies of the radio continuum emission from M 31. By observing the total and polarized emission at several wavelengths, the thermal and nonthermal contributions can be separated and Faraday rotation measures can be obtained. In this paper we focus on the polarized emission from the disk of M 31 at wavelengths between λ20 cm and λ6 cm.

Early high-resolution surveys of M 31 between λ74 cm and λ6 cm (Pooley 1969; Berkhuijsen & Wielebinski 1974; Berkhuijsen et al. 1983) showed the total emission mainly concentrated in a ring-like structure at about 50′ (≃10 kpc) from the centre. This ring of bright emission is also conspicuous in Hα (Devereux et al. 1994), FIR (Walterbos & Schwering 1987), H I (Emerson 1974; Brinks & Shane 1984) and CO (Koper et al. 1991). Optical images of M 31 as well as highly resolved (≲1′) maps in H I (Braun 1990), CO (Guélin et al. 2000), FIR (Haas et al. 1998), Hα (Walterbos 2000) and radio continuum (Beck et al. 1998) reveal that the emission ring consists of several tightly-wound spiral arms containing the main sites of star formation in the galaxy. Therefore, we shall refer to it as the "ring".

Polarized radio emission from M 31 was first detected by Beck et al. (1978) at λ11 cm with the 100-m Effelsberg telescope of the MPIfR. The complete survey at this wavelength (Beck et al. 1980) showed that the polarized emission is also concentrated in the "ring". From a detailed analysis, Beck (1982) concluded that the observed polarization angles at λ11 cm are consistent with a regular magnetic field oriented along the "ring". For the area within 30′ from the minor axis this result was confirmed by the first polarization observations at λ6 cm with the Effelsberg telescope (Berkhuijsen et al. 1987) and with the VLA at λ20 cm (Beck et al. 1989). However, for a proper analysis of the structure of the magnetic field in M 31 complete polarization surveys at several wavelengths are

Send offprint requests to: E. M. Berkhuijsen,
e-mail: eberkhuijsen@mpifr-bonn.mpg.de

[1] We use this classical distance value to enable direct comparisons with our earlier work. Recent distance determinations based on Cepheids yielded 780 kpc (Stanek & Garnavich 1998). See the end of Sect. 1 for scaling laws.

Table 1. Adopted positional data on M 31.

Position of the nucleus[1]	
$\alpha(1950) = 00^h40^m01^s.8$	$\delta(1950) = +40°59'46''$
$\alpha(2000) = 00^h42^m46^s.05$	$\delta(2000) = +41°16'12''$
Position angle of major axis	37°
Inclination[2]	78° (0° is face-on)
Distance[3]	690 kpc

[1] Pooley (1969). [2] Braun (1991). [3] G. and A. de Vaucouleurs (1964).

required. A survey at λ20 cm made with the VLA-D array with a resolution of 45″ and combined with an Effelsberg map at the same wavelength was published by Beck et al. (1998). It shows significant structure in the polarization angles in the "ring" on scales of several arcminutes, probably due to variations in Faraday rotation. Here we present a new λ6 cm survey obtained with the Effelsberg telescope with a resolution of 2′.4. Some preliminary results were discussed by Han et al. (1998) and Beck (2000).

The polarization surveys at $\lambda\lambda$6 cm, 11 cm and 20 cm have been combined to develop a model of the structure of the magnetic field in M 31 (Fletcher et al. 2000; Fletcher et al. 2003). In the present paper we discuss the distributions of thermal emission, nonthermal emission, polarized emission, rotation measure and depolarization across M 31 and what they can tell us about the magnetic field without detailed modelling.

The paper is organized as follows: in Sect. 2 we describe the observations and reduction and present the maps of total and polarized emission. In Sect. 3 we derive a spectral index map between λ20 cm and λ6 cm at 3′ resolution and the resulting distributions of thermal and nonthermal emission. The distributions of the polarized emission and degree of polarization at λ6 cm we discuss in Sect. 4, and the variations of rotation measures and depolarization between λ11 cm and λ6 cm across M 31 we present in Sect. 5. Section 6 gives a summary of our results.

Throughout this paper we use the positional data on M 31 as given in Table 1.

Scaling laws. For an adopted distance D to M 31 other than 690 kpc used here, linear scales within M 31 and the linear resolution of the maps scale with D. Directly observed quantities like the intensity of emission (=surface brightness), integrated flux density, polarization angles and rotation measure are independent of D. Quantities derived from ratios like spectral index, thermal fraction of the emission, degree of polarization and the amount of depolarization are also distance independent.

2. Observations

M 31 was observed at λ6.2 cm during three nights in August 1996 using the 4850 MHz HEMT receiver (30 K system temperature, 500 MHz bandwidth, $T_b/S = 2.55$ K Jy^{-1}, where T_b is the main beam brightness temperature and S the corresponding flux density) installed in the secondary focus of the 100-m Effelsberg radio telescope. A field of 150′ along the major axis (X) and 70′ along the minor axis (Y), centred on the nucleus of M 31, was scanned at a speed of 1°/min under excellent weather conditions. We obtained 10 coverages (5 coverages scanned in X and 5 in Y) with a typical sensitivity of 2 mJy/beam area in total power and 1 mJy/beam area in polarization. The beamwidth at λ6.2 cm is 2′.4 which corresponds to 480 pc × 2310 pc^2 in the plane of M 31.

Table 2. Flux densities I_6, degrees of polarization p_6 and polarization angles χ_6 of point sources in the M 31 field at λ6.2 cm. The 37W numbers are from the catalogue of Walterbos et al. (1985).

Source 37W	I_6 (mJy)	p_6 (%)	χ_6 (°)
45	24.8 ± 1.4	11.3 ± 0.7	91 ± 2
50	21.8 ± 1.2	12.3 ± 1.9	171 ± 4
83	32.9 ± 1.8	5.9 ± 0.5	52 ± 2
91	29.9 ± 1.5	5.5 ± 0.6	27 ± 4
115	133 ± 7	5.4 ± 0.2	79 ± 1
131	28.4 ± 1.4	5.4 ± 0.6	39 ± 3
168	24.2 ± 1.3	9.1 ± 0.7	96 ± 2
172	77 ± 4	2.8 ± 0.2	61 ± 2
175	31.5 ± 1.6	7.5 ± 0.5	167 ± 2
235	48.5 ± 2.8	6.0 ± 0.4	149 ± 2

3C 138 and 3C 286 were observed for calibration of flux density and polarization angle. Their absolute fluxes are uncertain by about ±5%, leading to a scale error in the λ6.2 cm data of the same amount; the error in their absolute polarization angles is ±1°.

The data reduction was performed using the NOD2 software package. The maps in X and Y were combined by applying the "basket-weaving" technique (Emerson & Gräve 1988), separately in Stokes parameters I, Q and U. The final maps in Q and U were combined to produce maps in polarized intensity and in polarization angle, taking into account the positive bias in polarized intensity due to noise, following the method proposed by Wardle & Kronberg (1974).

The rms noise in the final maps is 0.5 mJy/beam area in total power and 0.25 mJy/b.a. in polarization, corresponding to 1.0 mK and 0.5 mK, respectively. These maps are presented in Figs. 1 and 2.

The total power map (Fig. 1) shows the well known, bright emission "ring" at about 10 kpc from the centre. The map is consistent with the earlier map of Berkhuijsen et al. (1983), but supersedes the old map because of its 3.5× higher sensitivity.

A number of polarized point sources are visible in the field (see Fig. 1); their flux densities and polarization angles are listed in Table 2.

The polarization map is shown in Fig. 2. The polarized emission is concentrated in the "ring", but the emission is not evenly distributed, the NE and SW quadrants being brighter than the other quadrants. The observed degree of polarization strongly varies across M 31 and reaches >50% in regions of high polarized intensity (see Sect. 4).

The B-vectors of polarized emission (observed E-vectors rotated by 90°) are nearly aligned with the "ring", indicating that the regular magnetic field component in the plane

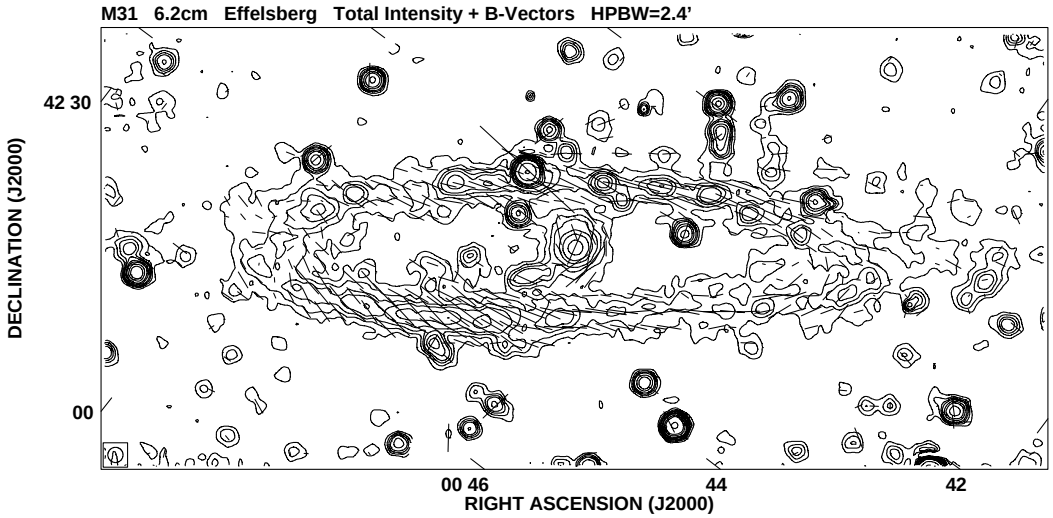

Fig. 1. Total power emission from M 31 at λ6.2 cm observed with the Effelsberg telescope, with apparent *B*-vectors of polarized intensity (*E*-vectors rotated by 90°) superimposed. The angular resolution is 2′.4. Contour levels are 2, 4, 6, 8, 12, 16, 24, 32, 64 and 128 mJy/beam area. The rms noise is 0.5 mJy/b.a. in total intensity and 0.25 mJy/b.a. in polarization. A vector of 5′ length represents a polarized intensity of 1.5 mJy/b.a. The beam area is shown in the lower left-hand corner. North is to the upper left and east is to the bottom left.

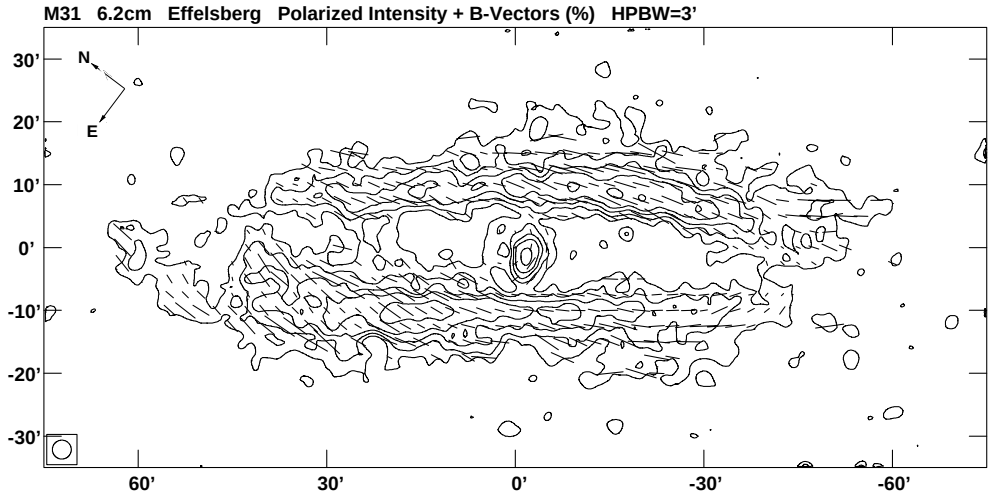

Fig. 2. Linearly polarized emission and apparent *B*-vectors of polarized intensity (*E*-vectors rotated by 90°) from M 31 at λ6.2 cm observed with the Effelsberg 100-m dish, smoothed to an angular resolution of 3′. Contour levels are 0.5, 1.0, 1.5, 2, 3 mJy/beam area. The rms noise is 0.25 mJy/b.a. The length of the vectors is proportional to the degree of polarization where 5′ represent 50%. The beam area is shown in the lower left-hand corner. Coordinates are with respect to the center of M 31 (see Table 1) using a position angle of the major axis of 37°. North is to the upper left and east to the bottom left.

of the sky could be aligned with the spiral arms forming the "ring". This confirms the conclusions of Beck (1982) and Berkhuijsen et al. (1987). After correction for Faraday rotation (see Sect. 5), the alignment of the "vectors" along the "ring" becomes tighter (see Fig. 10).

3. Distributions of spectral index, thermal and nonthermal emission

In order to derive the degree of polarization of the nonthermal emission, the two components contributing to the total power emission, nonthermal (synchrotron) and thermal (free-free) emission, must be separated. This is possible if data at two or more frequencies are available and the spectral index of the nonthermal emission, α_n ($S_n \propto \nu^{-\alpha_n}$), is known. We estimated α_n in two ways: from the spectrum of the integrated emission and from the spectral index map of the total emission.

3.1. Spectrum of the integrated emission

The spectrum of the integrated emission of M 31 was obtained from five recent surveys with angular resolutions ≤5′ (see Table 3). From each survey all point sources with flux densities larger than 40 mJy at 408 MHz were subtracted, the same criterion as was used by Beck & Gräve (1982). Most of these sources are unrelated to M 31. Assuming an inclination of the plane of M 31 of 78°, the maps were integrated out to a radial distance of 16 kpc ($X = 80'$) from the centre, an area

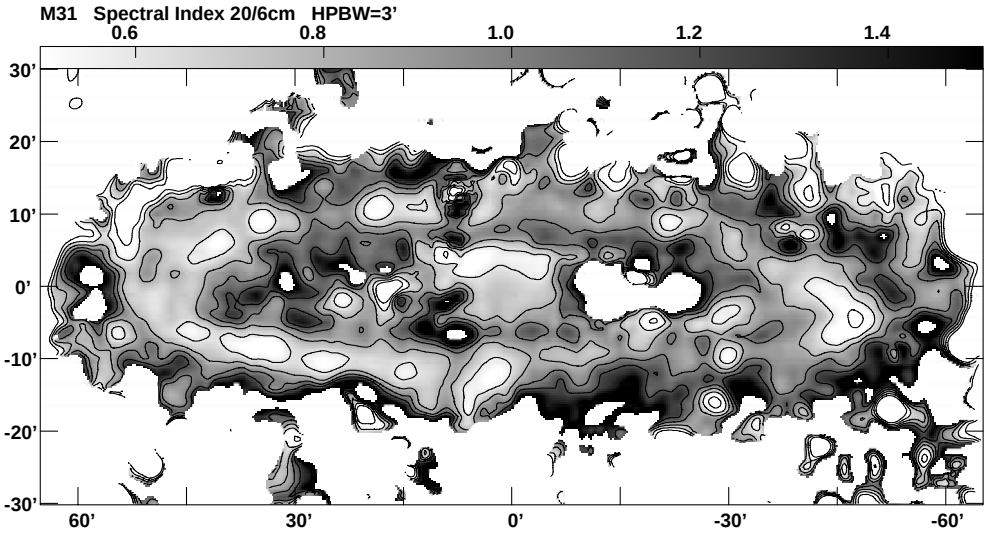

Fig. 3. Distribution of the flux-density spectral index between λ20.5 cm and λ6.2 cm, $\alpha(20, 6)$. Contour levels are 0.4, 0.6, 0.8, 1.0 and 1.2. Areas of flat spectrum ($\alpha < 0.6$) occur on regions of star formation in the emission ring (Fig. 1) and on an inner arm west of the nucleus. The angular resolution is 3′.

Table 3. Integrated flux densities of M 31.

ν [1] (MHz)	Telescope	Resolution (′)	Sources subtracted S (mJy) [2]	$S_{\rm int}(R \le 16$ kpc) (mJy) [3]	Reference
327	Westerbork	1.65×2.52	>47	14 800 ± 1100	Golla (1989)
408	Cambridge+W'bork	4/5	>40	11 200 ± 810	Pooley (1969), Beck & Gräve (1982)
1465	VLA+Effelsberg	0.75	>15	4840 ± 480	Beck et al. (1998)
2702	Effelsberg	4.4	>10	2630 ± 340	Beck et al. (1980)
4850	Effelsberg	2.4	> 6	1790 ± 200	This paper

[1] ν = frequency of observations; [2] S = flux density of subtracted point sources; [3] $S_{\rm int}$ ($R \le 16$ kpc) = flux density of M 31 integrated over the radius interval R = 0–16 kpc.

covered by four of the surveys. The λ6.2 cm map extends only to $X = |75'|$, therefore the integrated flux density at this wavelength may be low by 1%. The resulting flux densities are listed in Table 3. A least-squares fit to the spectrum of the integrated flux densities yields a spectral index $\alpha = 0.77 \pm 0.04$. A numerical fit of the equation $S(\nu) = S_{\rm th}(\nu)\nu^{-0.1} + S_{\rm n}(\nu)\nu^{-\alpha_{\rm n}}$, where $S(\nu)$, $S_{\rm th}(\nu)$ and $S_{\rm n}(\nu)$ are the total, thermal and nonthermal flux densities at a frequency ν (Klein et al. 1984), to the data in Table 3 yields $\alpha_{\rm n} = 1.0 \pm 0.2$ and a thermal fraction $S_{\rm th}/S$ at 1 GHz $f_{\rm th}(1{\rm GHz}) = 0.24 \pm 0.18$. This corresponds to a thermal fraction at λ6.2 cm of 0.40 ± 0.06 if only the error in α is used, and of 0.4 ± 0.2 if the uncertainty in $\alpha_{\rm n}$ is also included.

3.2. Distributions of spectral index, thermal emission and nonthermal emission

The spectral index distribution (see Fig. 3) was derived from the surveys with the highest resolutions, the VLA+Effelsberg map at λ20.5 cm and the Effelsberg map at λ6.2 cm, both without point sources unrelated to M 31 and smoothed to a beamwidth of 3′. The spectral index was only calculated for points with intensity larger than twice the noise level, in both maps.

The spectral index varies between about 0.4 at bright regions in the emission "ring" containing young stars and H II regions, and values >1.0 at small radii inside the ring and at large radii, especially near the southern major axis on the outer side of the "ring". Interestingly, the flat-spectrum strip near the nucleus running parallel to the major axis at $Y \simeq +5'$ coincides with an inner spiral arm apparent in CO (Nieten et al. 2000) and dust (Berkhuijsen et al. 2000). Spectra in the southern half of M 31 are generally steeper than in the northern half, a feature also observed by Beck & Gräve (1982) between λ74 cm and λ11 cm. In between the star-forming regions in the emission ring the spectral index increases to >0.9. As most of the relativistic electrons originate from supernovae in star-forming regions, this indicates a steepening of their spectrum from ~0.5 at their place of origin to >0.9 about 1 kpc away, which is generally attributed to energy-dependent diffusion. Steep spectra away from star-forming regions will occur in regions of purely nonthermal emission, where $\alpha = \alpha_{\rm n}$. Figure 3 shows that $\alpha_{\rm n} \simeq 0.95$–$1.05$ in the northern half and $\alpha_{\rm n} \simeq 1.0$–$1.1$ in the southern part. Hence a mean value of $\alpha_{\rm n}(20, 6) = 1.0 \pm 0.1$ is a good estimate and in good agreement with the value derived from the spectrum of the integrated emission covering a much larger wavelength range.

Table 4. Integrated flux densities (mJy) of emission components in M 31 at λ6.2 cm for galactic radii $R < 16$ kpc.

Component	Total	North	South	N/S [1]
Total emission [2]	1790 ± 200	990 ± 100	800 ± 100	1.24 ± 0.04
Thermal emission [2]	500 ± 360	320 ± 180	180 ± 180	>1.4 [5]
Nonthermal emission [2]	1290 ± 360	670 ± 180	620 ± 180	1.08 ± 0.03
Polarized emission [2]	390 ± 80	200 ± 40	190 ± 40	1.05 ± 0.02
$\alpha(20.5, 6.2)$ [3]	0.83 ± 0.13	0.80 ± 0.12	0.87 ± 0.14	
$f_{\rm th}(6.2)$ for $\alpha_{\rm n} = 1.0$ [3]	0.28 ± 0.20	0.32 ± 0.17	0.22 ± 0.22	
$p_{\rm n}(6.2)$ [3,4]	0.3 ± 0.2	0.3 ± 0.2	0.3 ± 0.2	

[1] N/S = ratio of integrated flux densities, North/South.
[2] Errors are *systematic* errors due to uncertainty in the zerolevel. As they have the *same* sign in North and South, they hardly affect the ratio N/S.
[3] Errors are conservative systematic errors following from the systematic errors in the flux densities.
[4] $p_{\rm n}$ = nonthermal degree of polarization = polarized/nonthermal emission.
[5] The computed value is $1.8^{+\infty}_{-0.4}$, hence >1.4.

Using the maps at λ20.5 cm and λ6.2 cm, the spectral index map of Fig. 3 and $\alpha_{\rm n} = 1.0$ we calculated the distributions of thermal fraction, thermal emission and nonthermal emission at λ6.2 cm. At points of low intensity ($<2\sigma$) where $\alpha(20, 6)$ is not available, the total emission at λ6.2 cm was assumed to be entirely nonthermal. As these points occur mainly in regions of low star formation, this procedure will have little effect on the distribution of thermal emission. Another source of error is the assumption of constant $\alpha_{\rm n}$. If in the star-forming regions, where the relativistic electrons originate, $\alpha_{\rm n} < 1.0$ we will overestimate the thermal emission from these regions and underestimate the nonthermal emission. For example, if $\alpha = 0.5$ and $\alpha_{\rm n} = 0.7$ the thermal fraction at λ6.2 cm is $f_{\rm th}(6.2) = 0.44$, whereas $\alpha_{\rm n} = 1.0$ would give $f_{\rm th}(6.2) = 0.72$ in this region. So locally in star-forming regions the thermal (nonthermal) emission may be overestimated (underestimated) by 50% or more. On the other hand, the linear resolution of the 3′ beam in M 31 is $600 \times 2890\,{\rm pc}^2$, too large to resolve supernova remnants. Therefore, this error should have little effect on the derived distributions of thermal and nonthermal emission.

In Fig. 4 we show the distribution of the thermal emission at λ6.2 cm superimposed onto the Hα map of Devereux et al. (1994) smoothed to the same resolution. The agreement is generally good. Star-forming regions are bright in both Hα and thermal radio. Comparison with the total power map in Fig. 1 shows that more than 70% of the emission is thermal in these regions, even 84% at the thermal maximum near the southwestern major axis ($X = -48'$, $Y = -5'$).

The distribution of the nonthermal emission at λ6.2 cm is presented in Fig. 5. It is remarkably smooth, much wider in galacto-centric radius and more diffuse than that of the thermal emission. This could be the result of the diffusion of the relativistic electrons away from their places of origin along a fairly regular magnetic field and a nearly constant total field strength (see Sect. 3.3). The highest intensities in the northeastern part of the ring are 9 mJy/b.a. whereas the thermal intensity reaches 12 mJy/b.a. Also in other bright regions the thermal emission is stronger than the nonthermal emission. In spite of this the thermal flux density integrated out to $R = 16$ kpc is less than half of the integrated nonthermal flux density (see Table 4).

3.3. Radial distributions

Already early radio continuum maps of M 31 showed stronger emission from the northern half (left of the minor axis) than from the southern half (right of the minor axis), an asymmetry also found for other constituents like H I and H II regions (Berkhuijsen 1977). Our Figs. 1 to 5 confirm this asymmetry; especially the northeastern quadrant is very bright.

Differences and similarities between the two halves of M 31 are better visible in radial profiles of the various emissions. Therefore we averaged the emission at λ20 cm and λ6.2 cm (both at 3′ resolution and without point sources) from each half in 1 kpc-wide rings around the centre in the plane of M 31, using an inclination angle $i = 78°$. From these average intensities we calculated the spectral index $\alpha(20, 6)$ and thermal fraction $f_{\rm th}(6.2)$ for each ring, again assuming $\alpha_{\rm n} = 1.0$ (see Sect. 3.1). For these calculations data points below 2σ were also used, yielding slightly higher values of $\alpha(20, 6)$ in low-density regions than obtained in the spectral index map of Fig. 3. The average thermal and nonthermal intensities at λ6.2 cm in a ring then are $\bar{S}_{\rm th}(6.2) = f_{\rm th}(6.2)\bar{S}(6.2)$ and $\bar{S}_{\rm n}(6.2) = (1 - f_{\rm th}(6.2))\bar{S}(6.2)$, where $\bar{S}(6.2)$ is the average intensity at λ6.2 cm of the total emission for that ring. The average polarized intensities were calculated from the polarization map (Fig. 2) after subtraction of polarized point sources. The resulting profiles are presented in Figs. 6 and 7.

The spectral index $\alpha(20, 6)$ (Fig. 6, top) varies between values around 0.7 at the bright "ring" of emission near $R = 10$ kpc in the north and values close to 1.1 near $R = 5$ kpc and at $R > 15$ kpc on both sides. The latter values suggest a mean value of the nonthermal spectral index $\alpha_{\rm n} = 1.05$, slightly higher than $\alpha_{\rm n} = 1.0$ assumed here, but still within the estimated error. At the bright "ring" of emission in the south $\alpha(20, 6) \simeq 0.82$, which is significantly steeper than in the north. The profiles show this difference more clearly than the spectral index map in Fig. 3. Also the central region has $\alpha(20, 6) \simeq 0.7$. This is consistent with the result of Walterbos & Gräve (1985) who found $\alpha = 0.75 \pm 0.05$ for the area $R < 1.2$ kpc in the frequency range 0.6–4.8 GHz.

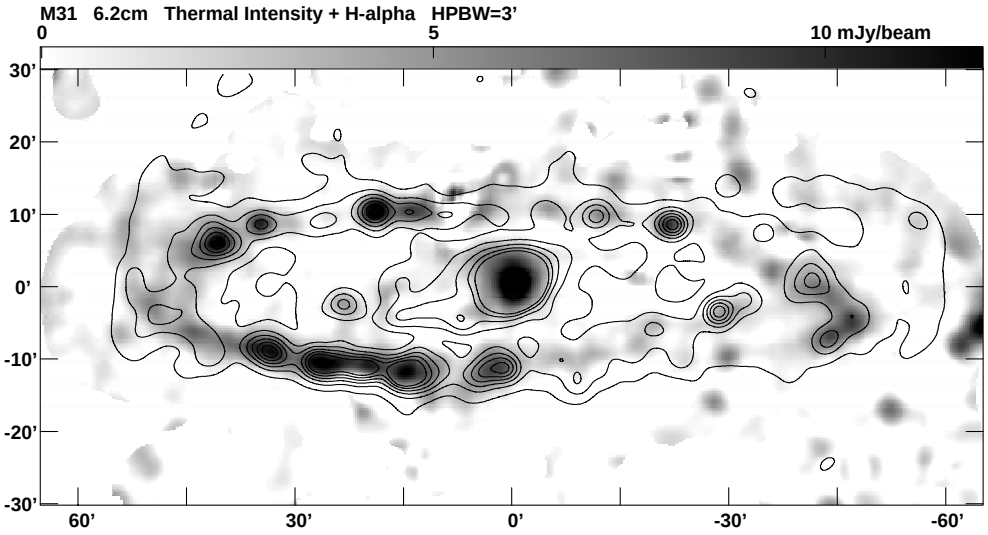

Fig. 4. Thermal emission from M 31 at λ6.2 cm (greyscale) obtained from the spectral index map shown in Fig. 3 and assuming a constant nonthermal spectral index $\alpha_n = 1.0$. Some contours of the Hα map of Devereux et al. (1994) are also shown. The angular resolution is 3′ for both maps.

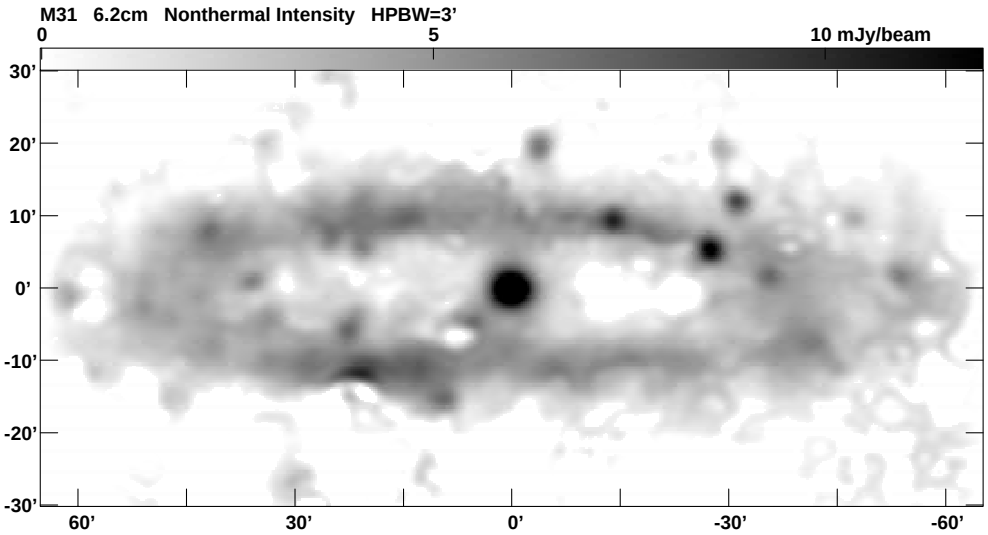

Fig. 5. Nonthermal emission from M 31 at λ6.2 cm obtained from the spectral index map shown in Fig. 3 and $\alpha_n = 1.0$. The angular resolution is 3′. The distribution is much smoother and broader in galacto-centric radius than that of the thermal emission shown in Fig. 4.

The profile of the thermal fraction at λ6.2 cm (Fig. 6, bottom) mirrors that of $\alpha(20, 6)$. The highest thermal fraction, $f_{th}(6.2) = 0.51$, occurs in the "ring" R = 10–11 kpc in the north, whereas on the southern part of the "ring" a value of only 0.30 is reached. In the inner few kpc $f_{th}(6.2) = 0.45$. We note that with $\alpha_n = 1.05$, the thermal fractions would be on average about 25% higher than obtained here.

Figure 7 shows the radial profiles of the total, nonthermal, thermal and polarized emission at λ6.2 cm. In all these constituents the bright emission "ring" is clearly visible with maxima near R = 10 kpc in the north and R = 9 kpc in the south. The polarized emission peaks between R = 8–10 kpc on both sides. We note that the difference in total intensity between the northern and southern part of the emission "ring" is entirely due to the difference in thermal emission, whereas the maximum intensities of both the nonthermal and the polarized emission are *very similar* in the two halves of M 31. This surprising result shows that local star formation does not necessarily lead to an increase of nonthermal emission in a star-forming region. This may be explained by the fast diffusion of relativistic electrons along the magnetic field that is nearly aligned with the "ring", in which case the magnetic field strength in the northern and southern parts of the ring must also be nearly the same. A further discussion of the physical implications of the symmetry in the profiles of nonthermal and polarized emission in Fig. 7 we defer to a later paper (Berkhuijsen & Beck, in prep.).

In Table 4 we compare the flux densities of the various emission components integrated within the radius R = 16 kpc in the plane of M 31. The northern half emits at least 40% more thermal radiation than the southern half, which largely accounts for the asymmetry in the total radio continuum emission, whereas the nonthermal components are equal to within

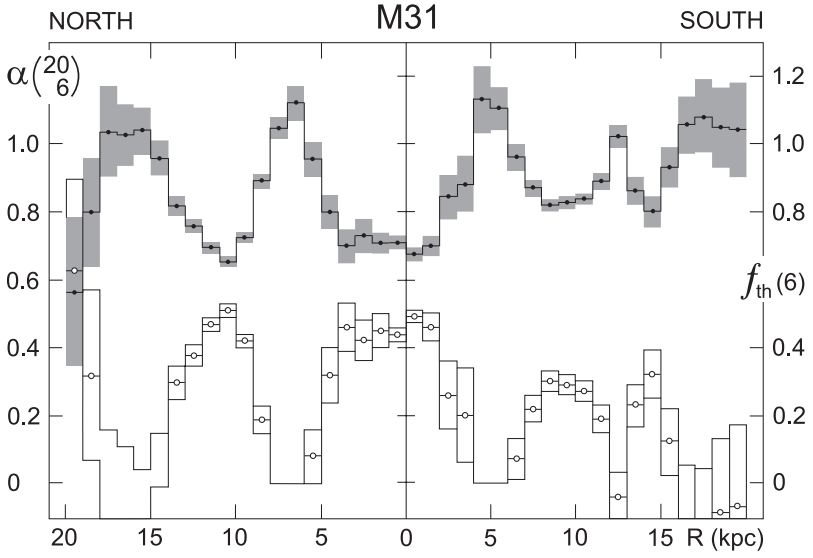

Fig. 6. Radial distributions of $\alpha(20, 6)$ (top) and the thermal fraction at λ6.2 cm, $f_{\rm th}(6)$ (bottom) for the northern and southern half of M 31. Average values are shown for 1 kpc-wide, semicircular rings in the plane of M 31 north and south of the minor axis, assuming an inclination angle of 78°. Boxes indicate the 1σ range.

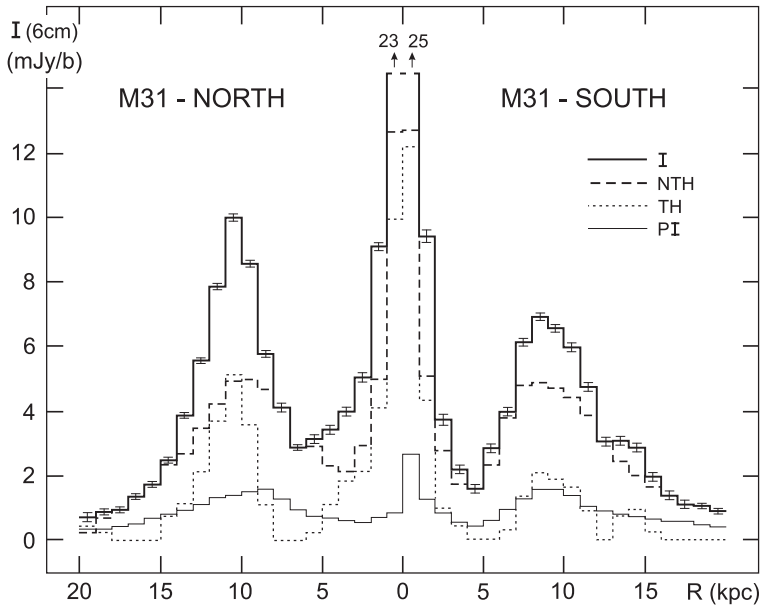

Fig. 7. Radial distributions for the northern and southern half of M 31 of the total emission, the nonthermal emission, the thermal emission and the polarized emission at λ6.2 cm.

8%. These properties are reflected in the values of $\alpha(20, 6)$, $f_{\rm th}(6.2)$ and the nonthermal degree of polarization $p_{\rm n}(6.2)$, also shown in Table 4.

4. Distribution of polarized emission

A grey-scale representation of the polarized emission is shown in Fig. 8. The distribution of the polarized emission, concentrated in the "ring", indicates that the regular magnetic field is nearly oriented along the spiral arms that form the bright emission "ring" (Beck 1982). As Faraday depolarization at λ6.2 cm is small the pattern directly shows the geometry of the regular field: in the NE and SW quadrants, where *PI* is maximum, the line of sight is perpendicular to the field, whereas in the other quadrants the minima in *PI* occur near the major axis where the line of sight is nearly parallel to the field. ($PI \propto B^2_{\rm reg\perp}$, where $B_{\rm reg\perp}$ is the transverse component of the regular magnetic field.) The shift between *PI* maxima (minima) and the minor (major) axis, also noted by Urbanik et al. (1994), indicates that the field is not exactly azimuthal in the plane of M 31. Thus, from an analysis of the variation of *PI* along the "ring" geometrical properties of the regular field can be determined.

This is illustrated in Fig. 12a, which shows the variation of *PI*(6.2) averaged in azimuthal sectors of 5° width in the plane of M 31 for the radial ring R = 8–12 kpc. The well defined maxima occur at the azimuthal angles $\theta \simeq 70°$ and $\theta \simeq 260°$. A fit of a double sine curve through the points gives mean positions for the maxima at $\theta = 77° \pm 7°$ and $257° \pm 7°$ yielding a pitch angle of the regular magnetic field of $-13° \pm 7°$. This value is in good agreement with earlier determinations from an analysis of the variation of polarization angles with azimuth at λ11 cm (Beck 1982; Ruzmaikin et al. 1990). We stress that at λ6.2 cm the strong variation of *PI* with azimuthal angle is entirely due to the geometrical effect of $B_{\rm reg\perp}$ varying with azimuth. Because the M 31 disk is not seen exactly edge-on, but under an inclination angle of 78°, $B_{\rm reg\perp}$ does not go to zero and some weak polarized emission is left near the major

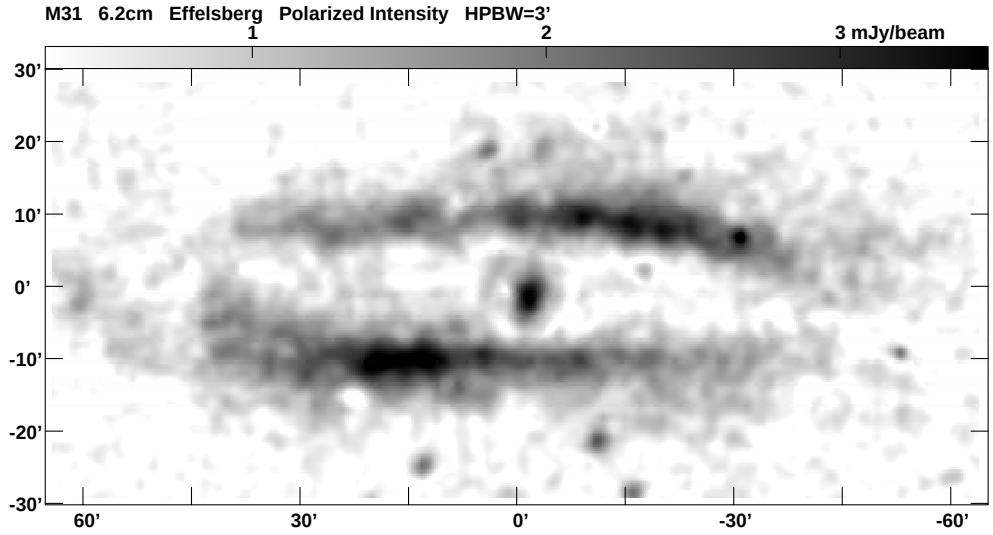

Fig. 8. Linearly polarized emission from M 31 at λ6.2 cm. Note the strong emission from the NE (lower left) and SW (upper right) quadrants and the minima near the major axis. The rms noise is 0.2 mJy/beam. The angular resolution is 3′.

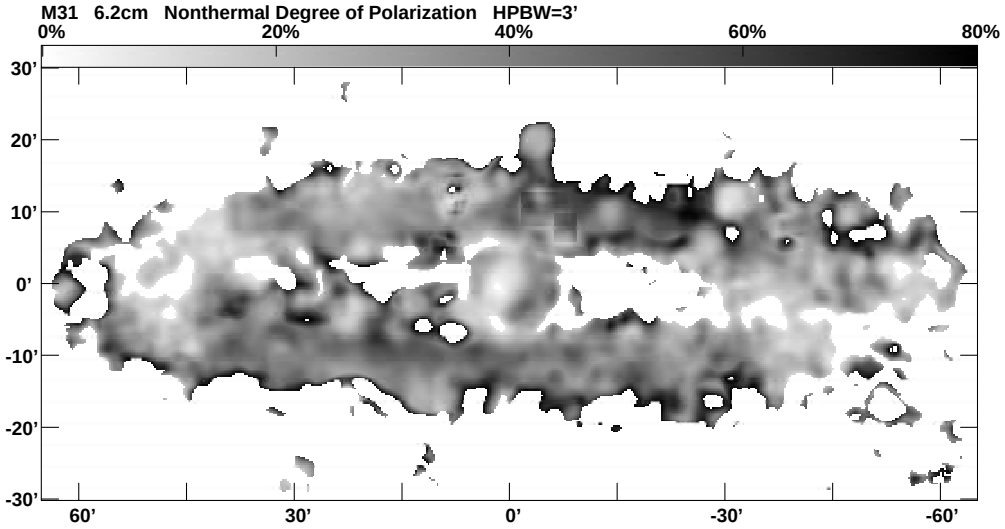

Fig. 9. Distribution of the nonthermal degree of polarized emission at λ6.2 cm, $p_{\rm n}(6.2) = PI(6.2)/NTH(6.2)$. The angular resolution is 3′. In the SW (upper right) and the NE (lower left) quadrant percentages of more than 50% are reached. The circular minima in the SW quadrant are due to some point sources left in the map of nonthermal emission.

axis. The mean polarized intensity is 1.4 mJy/beam for the ring R = 8–12 kpc, in agreement with Fig. 7.

In Fig. 9 we present the distribution of the nonthermal degree of polarization at λ6.2 cm, $p_{\rm n}(6.2)$, the ratio of polarized intensity (Fig. 8) and nonthermal intensity (Fig. 5). We calculated $p_{\rm n}(6.2)$ only where both intensities are higher than twice the noise level.

The symmetry in the polarization map is reflected in the degrees of polarization, which are high in the southwestern and northeastern quadrants, and low near the major axis. Values $\gtrsim$50% occur in an extended area in the southwest and in some places in the northeast. As the maximum intrinsic degree of polarization, p_0, is 75% the high degree of polarization in these regions implies an extremely regular magnetic field. As Faraday effects are small at λ6.2 cm, the depolarization from 75% to 50% must be mainly due to tangling of the magnetic field on unresolved scales leading to wavelength-independent depolarization (Burn 1966; Sokoloff et al. 1998). Then $p_{\rm n}(6.2) = p_0 B^2_{\rm reg\perp}/(B^2_{\rm reg\perp}+B^2_{\rm tur\perp}) \gtrsim 0.5$ yields $B_{\rm reg\perp}/B_{\rm tur\perp} \gtrsim 1.4$, where $B_{\rm tur\perp}$ is the transverse component of the turbulent magnetic field. Thus in M 31 the transverse component of the regular field is stronger than that of the turbulent field, quite an exceptional situation in a spiral galaxy. As the large-scale variation of $PI(6.2)$ along the "ring" has a geometrical cause, the exceptional regularity of the field probably holds everywhere in the "ring".

5. Rotation measures and depolarization

The distribution of the rotation measures between λ11.1 cm and λ6.2 cm, $RM(11,6)$, is presented in Fig. 11. We used the λ11 cm polarization map of Beck et al. (1980) and smoothed both data sets to an angular resolution of 5′. For the calculation of $RM(11,6)$ only data above 3σ in PI were

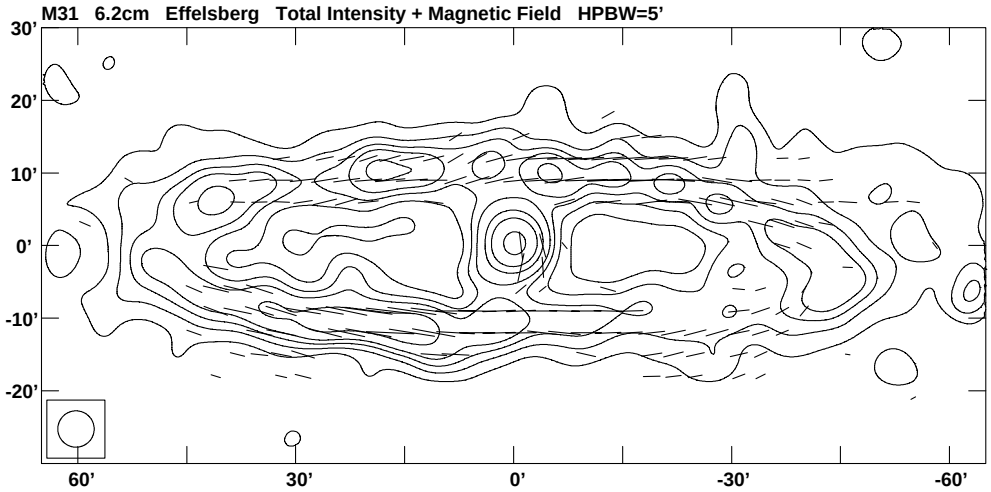

Fig. 10. Total emission (contours) and polarized emission (B-vectors) from M 31 at λ6.2 cm, smoothed to an angular resolution of 5′. Contour levels are 5, 10, 15, 20, 30, 40 and 60 mJy/beam area. A vector length of 10′ represents a polarized intensity of 12 mJy/b.a. The E-vector orientations are corrected for Faraday rotation and rotated by 90°, thus they show the orientation of the regular magnetic field component in the plane of the sky, $B_{\mathrm{reg}\perp}$.

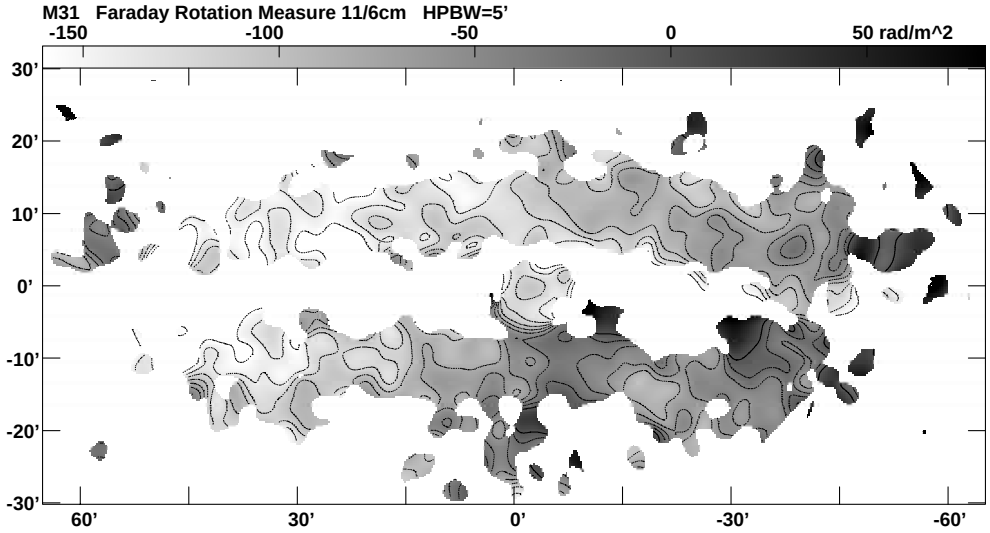

Fig. 11. Distribution of the rotation measure between λ11.1 cm and λ6.2 cm, $RM(11,6)$, across M 31. Contour levels of −160, −140, −120, −100, −80, −60, −40, −20 and 0 rad m^{-2} are shown. The foreground rotation measure caused by the Milky Way has not been subtracted. Note the gradient in $RM(11,6)$ from values near 0 rad m^{-2} on the southern major axis ($X < 0'$) to values near −180 rad m^{-2} on the northern major axis ($X > 0'$). The angular resolution is 5′.

used. We corrected the observed polarization angles at λ6.2 cm (at a resolution of 5′) for Faraday rotation ($\Delta\psi = RM\lambda^2$), using the distribution of $RM(11,6)$ of Fig. 11. As the polarized disk of M 31 is transparent at λ11 cm and λ6 cm (Fletcher et al. 2003), this distribution represents the full observable $RM(11,6)$ along the line of sight and gives the correct values of $\Delta\psi$. Thus the vectors shown in Fig. 10 represent the true orientations of $B_{\mathrm{reg}\perp}$ in the sky. The alignment of the vectors with the "ring" of emission is striking.

On both sides of the major axis in Fig. 11 the RMs show a gradual change from values around 0 rad m^{-2} near the southern major axis to values around −180 rad m^{-2} near the northern major axis. Especially in the southern half the eastern part of the "ring" shows less negative values than the western part. Note that the foreground rotation measure caused by the Milky Way, RM_{FG}, has not been subtracted. As $RM_{\mathrm{FG}} \simeq -90$ rad m^{-2} (Beck 1982; Han et al. 1998) the rotation measure intrinsic to M 31, $RM_{\mathrm{i}}(11,6)$, reaches zero near $X = 15'$, $Y = -10'$ in the NE (azimuthal angle ≃80°) and $X = -15'$, $Y = +10'$ in the SW (azimuthal angle ≃260°). These are the positions where we are indeed looking perpendicular to the regular magnetic field in M 31 and the polarized intensity is highest (see Sect. 4).

The systematic variation of $RM(11,6)$ along the "ring" is better visible in Fig. 12b, which shows $RM(11,6)$ averaged in 10°-wide sectors in the radial ring R = 8–12 kpc. The variation can be well fitted by a sine curve with an amplitude of 78 rad m^{-2} and a zero line at $RM_{\mathrm{FG}} = -92 \pm 3$ rad m^{-2}, in agreement with earlier determinations. Since RM is proportional to the parallel component of the regular magnetic field, it is a measure of $B_{\mathrm{reg}\parallel}$. $RM_{\mathrm{i}}(11,6)$ will be zero when the line

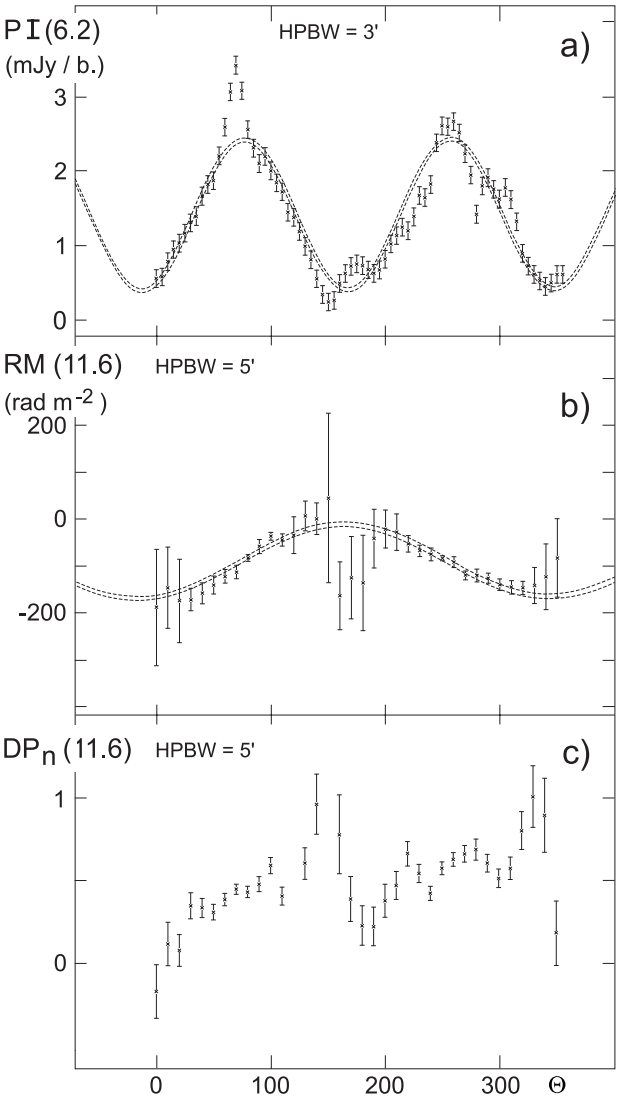

Fig. 12. Variations with azimuth along the radial ring R = 8–12 kpc of **a)** $PI(6.2)$, **b)** $RM(11,6)$ and **c)** $DP_{\rm n}(11,6)$. Mean values are shown for sectors of 5° width in the plane of M 31 in **a)** and of 10° width in **b)** and **c)**. The azimuthal angle θ is counted counterclockwise from the northern major axis. An inclination angle of 78° was assumed for the plane of M 31. The dashed curves in **a)** and **b)** indicate the $\pm\sigma$ range of the fit.

of sight is perpendicular to $B_{\rm reg}$. This occurs for the azimuthal angles 73° ± 4° and 253° ± 4°, in good agreement with the values of 77° ± 7° and 257° ± 7° found from the fit to the polarized intensities in Fig. 12a (see Sect. 4). This shows that (1) the variation of $RM_{\rm i}(11,6)$ along the emission ring of M 31 can be explained by the geometric variation of $B_{\rm reg\|}$ along the "ring", and (2) $B_{\rm reg\|}$ and $B_{\rm reg\perp}$ are indeed components of the same regular magnetic field that is nearly aligned with the spiral arms that form the "ring" with an average pitch angle of about −15°. Some deviations in RM from the fitted curve near the southern major axis ($\theta \cong 180°$) indicate local field components with larger pitch angles.

It is interesting that $|RM_{\rm i}|$ is not increased at positions of strong thermal emission (compare Fig. 4). This indicates that discrete H II regions of high electron density, which emit 80% of the thermal emission (Walterbos & Braun 1994) hardly contribute to $RM_{\rm i}$ at this resolution, probably because of their small filling factors. Thus the observed rotation measures are mainly produced in the extended diffuse ionized gas in the "ring". This may also be the case in the Milky Way. Heiles (1976) pointed out that RMs of extragalactic sources and pulsars must largely originate in the diffuse ionized gas.

Comparison of the nonthermal polarization percentages at λ11.1 cm and λ6.2 cm yields information on the λ-dependent depolarization. In Fig. 13 we show the distribution of $DP_{\rm n}(11,6) = p_{\rm n}(11)/p_{\rm n}(6)$, the nonthermal depolarization between λ11.1 cm and λ6.2 cm, at a resolution of 5′. By taking the ratio of the percentages the λ-independent depolarization cancels and only the λ-dependent part remains. At λ6.2 cm Faraday depolarization is negligible, thus values of $DP_{\rm n}(11,6) < 1$ indicate Faraday depolarization at λ11.1 cm. Along the emission "ring" values vary between 0.2 in some places in the northeastern quadrant and nearly 1 near the major axis and the nuclear region. The far side ($Y < 0'$) is more depolarized than the near side ($Y > 0'$).

We note that the distribution of $DP_{\rm n}(11,6)$ is not correlated with that of the thermal emission shown in Fig. 4. Hence, like the rotation measures, also the Faraday depolarization must mainly occur in the extended, diffuse ionized gas in M 31. If this is indeed the case one would expect some kind of anticorrelation between $RM_{\rm i}(11,6)$ and $DP_{\rm n}(11,6)$. Figure 14 shows a combination of the two distributions, which are represented by thick and thin contours, respectively. It is remarkable that the contours of $RM_{\rm i}(11,6)$ and $DP_{\rm n}(11,6)$ tend to be perpendicular to each other at their crossing points, a phenomenon also observed for M 51 (Horellou et al. 1992). This suggests that gradients in $RM_{\rm i}$ on small scales, i.e. across the beam, are an important cause of Faraday depolarization in M 31 at λ11.1 cm. The same mechanism appeared to be largely responsible for the depolarization between λ20 cm and λ6 cm in the southwestern quadrant of M 31 (Berkhuijsen & Beck 1990).

Figure 12c shows $DP_{\rm n}(11,6)$ for 10°-wide sectors in the radial ring R = 8–12 kpc. In the far side of the disk (azimuthal angles 30°–120°) the mean value is $\overline{DP}_{\rm n}(11,6) = 0.39 \pm 0.03$, whereas in the near side (azimuthal angles 210°–300°) $\overline{DP}_{\rm n}(11,6) = 0.56 \pm 0.03$. This large-scale difference may indeed be due to the steeper gradient in $RM_{\rm i}$ in the far side ($18 \pm 3\,{\rm rad\,m^{-2}\,sector^{-1}}$) than in the near side ($-11 \pm 2\,{\rm rad\,m^{-2}\,sector^{-1}}$), visible in Fig. 12b. Interestingly, near the major axis where $|RM_{\rm i}|$ is largest $DP_{\rm n}(11,6) \simeq 1$, which means that differential Faraday depolarization in M 31 is negligible at λ11 cm.

A detailed model of the magnetic field structure in M 31, including depolarization effects, is presented by Fletcher et al. (2000, 2003).

6. Conclusions

We used the 100-m radio telescope at Effelsberg for observations of M 31 at λ6.2 cm with high sensitivity in total and polarized emission; the angular resolution is 2′.4 (Figs. 1 and 2). For further analysis we subtracted point sources unrelated to M 31 and smoothed the distributions of total and polarized emission

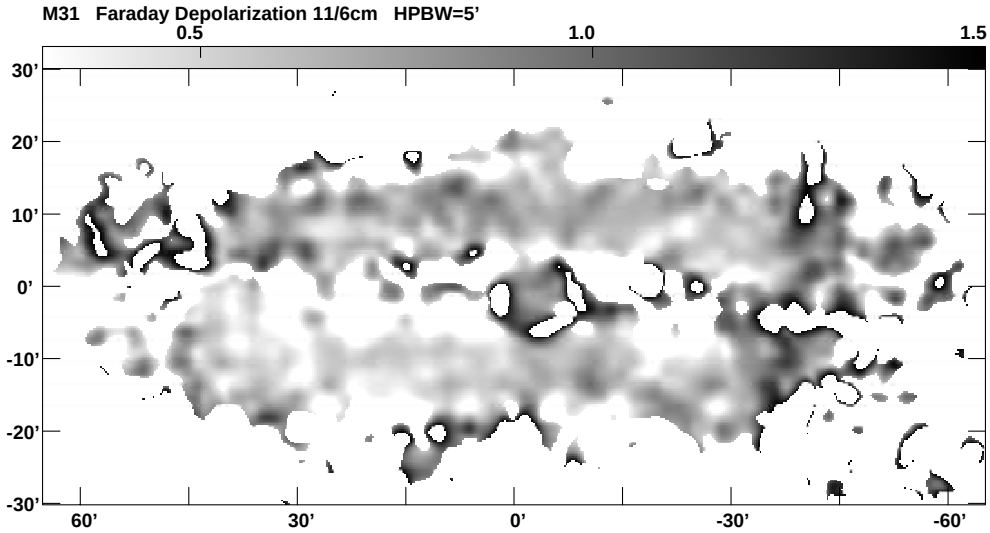

Fig. 13. Distribution of the nonthermal depolarization between λ11.1 cm and λ6.2 cm, $DP_{\rm n}(11,6)$, across M 31. $DP_{\rm n}(11,6) = 1$ means no Faraday depolarization between λ11.1 cm and λ6.2 cm. Note the somewhat lower values in the far side (below the major axis) compared to the near side (above the major axis) of the M 31 disk.

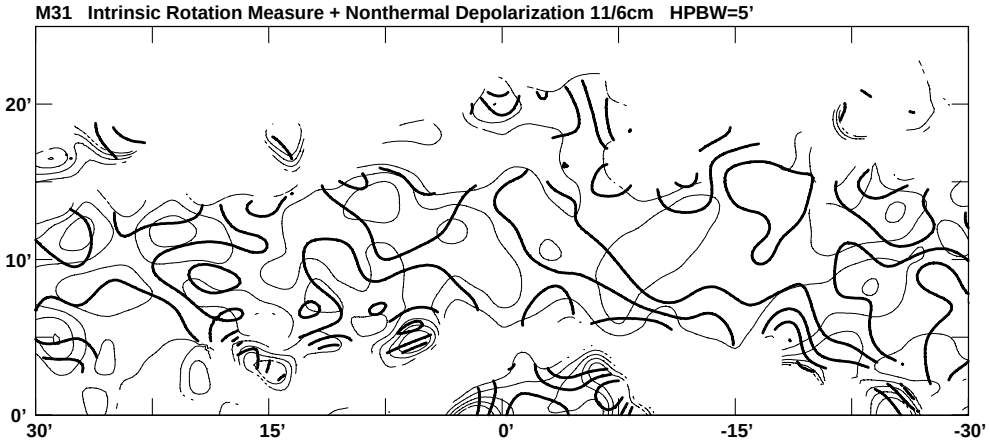

Fig. 14. Combined plot of the distributions of $DP_{\rm n}(11,6)$ (thin lines) and $RM_{\rm i}(11,6)$ (thick lines) shown in Figs. 13 and 11, respectively. For clarity only an area around the western minor axis ($Y > 0$) is shown. Contour levels of $DP_{\rm n}(11,6)$ are 0.1 step 0.2 to 1.3 and of $RM_{\rm i}(11,6)$ −70 step 20 to +30 rad m^{-2}. $RM_{\rm FG} = -90$ rad m^{-2} has been subtracted. The angular resolution is 5′. Thin and thick lines tend to be perpendicular to each other at their crossing points. This suggests that small-scale gradients in $RM(11,6)$ are an important cause of Faraday depolarization between λ11.1 cm and λ6.2 cm.

to a half-power beamwidth of 3′. Our main results may be summarized as follows.

1. Both the spectrum of the integrated emission for $R < 16$ kpc and the spectral index map between λ20.5 cm and λ6.2 cm (Fig. 3) indicate a nonthermal spectral index of $\alpha_{\rm n} = 1.0 \pm 0.2$ and a fraction of thermal emission at λ6.2 cm of 0.4 ± 0.2. The spectral index of the integrated emission is $\alpha = 0.77 \pm 0.04$ out to this radius.

2. Using the spectral index map and the total power map at λ6.2 cm we derived maps of thermal and nonthermal emission at λ6.2 cm, assuming $\alpha_{\rm n} = 1.0$ everywhere in M 31. The distribution of the thermal emission at the resolution of 3′ is very similar to that of the Hα emission (Devereux et al. 1994) smoothed to the same beamwidth (Fig. 4). The thermal emission is mainly confined to the spiral arms that form the "ring" of bright emission in M 31. The nonthermal emission is much more widely distributed and remarkably smooth (Fig. 5), probably due to fast diffusion of the relativistic electrons away from their places of origin along the regular magnetic field of nearly constant strength.

3. The radial profiles of the various emission components, plotted separately for the northern and southern half of M 31 (i.e. for $X > 0'$ and $X < 0'$, respectively) in Fig. 7, revealed that the stronger total emission in the northern part is entirely due to stronger thermal emission. The profiles of both nonthermal and polarized emission are nearly identical on either side of the minor axis. This suggests that recent star formation does not enhance the nonthermal emission locally.

The second part of the paper concerns properties of the polarized disk in M 31.

4. At an angular resolution of 5′, the projected B-vectors of polarized emission (=E-vectors corrected for Faraday rotation and rotated by 90°) are nearly aligned with the emission "ring" (Fig. 10).

5. The polarized emission at λ6.2 cm strongly varies along the emission "ring" (Fig. 8) because of the varying angle between the line of sight and the direction of the regular magnetic field $B_{\rm reg}$. The variation in the radial ring R = 8–12 kpc (Fig. 11a) shows maxima at azimuthal angles 77° ± 7° and 257° ± 7°, where we are looking perpendicular to the regular field that is nearly aligned with the arms forming the emission "ring" with an average pitch angle of about −15° (see also conclusion 7).
6. The nonthermal degree of polarization in M 31 is high (Fig. 9). At λ6.2 cm it reaches values >50% in the regions of maximum polarization. This implies a ratio of the transverse components of the regular and turbulent magnetic field of $\gtrsim$1.4, *an extraordinary situation in a spiral galaxy*.
7. The distribution of the rotation measures between λ11.1 cm and λ6.2 cm at a resolution of 5′ confirms the geometry of the regular magnetic field along the "ring" (Fig. 11). The variation of $RM(11,6)$ in the radial ring R = 8–12 kpc (Fig. 12b) yields a foreground rotation measure in the Milky Way of -92 ± 3 rad m^{-2} and a maximum rotation measure in M 31 of $|RM_{\rm i}(11,6)| = 78$ rad m^{-2}. $RM_{\rm i}(11,6) = 0$ occurs at azimuthal angles 73° ± 4° and 253° ± 4°, in good agreement with the positions of maximum polarized emission. At these positions the line-of-sight component of the regular field $B_{\rm reg\|} = 0$. Hence polarized emission and $RM_{\rm i}(11,6)$ indeed originate in the same regular magnetic field.
8. The ratio of the degrees of polarization at λ11.1 cm and λ6.2 cm, $DP_{\rm n}(11,6) = p_{\rm n}(11)/p_{\rm n}(6)$, is a measure of Faraday depolarization. Typical values are 0.1 to 0.7 (Fig. 13), with somewhat lower values in the eastern than in the western half of M 31. The variation of $DP_{\rm n}(11,6)$ in the radial ring R = 8–12 kpc (Fig. 12c) suggests that gradients in $RM_{\rm i}(11,6)$ (Fig. 12b) are responsible for the depolarization at λ11.1 cm. This is also suggested by the fact that contours of $RM(11,6)$ are largely perpendicular to contours of $DP_{\rm n}(11,6)$ at their crossing points (Fig. 14).
9. It is interesting that none of the distributions of $PI(6.2)$, $p_{\rm n}(6.2)$, $DP_{\rm n}(11,6)$ and $RM_{\rm i}(11,6)$ shows any relation to thermal emission. This indicates that on scales $\gtrsim$600 pc the dense H II regions responsible for 80% of the thermal emission do not cause significant Faraday rotation or depolarization, probably because of their small filling factors. Therefore, rotation measures and Faraday depolarization must originate in the diffuse ionized gas in M 31 which is widespread.

Acknowledgements. We thank Dr. A. Fletcher for valuable discussions and critical reading of the manuscript, and the referee, Dr. A. Shukurov, for useful comments.

References

Beck, R. 1982, A&A, 106, 121
Beck, R. 2000, in The Interstellar Medium in M 31 and M 33, Proc. 232. WE-Heraeus Seminar, ed. E. M. Berkhuijsen, R. Beck, & R. A. M. Walterbos (Aachen: Shaker), 171
Beck, R., & Gräve, R. 1982, A&A, 105, 192
Beck, R., Berkhuijsen, E. M., & Wielebinski, R. 1978, A&A, 68, L27
Beck, R., Berkhuijsen, E. M., & Wielebinski, R. 1980, Nature, 283, 272
Beck, R., Loiseau, N., Hummel, E., et al. 1989, A&A, 222, 58
Beck, R., Berkhuijsen, E. M., & Hoernes, P. 1998, A&AS, 129, 329
Berkhuijsen, E. M. 1977, A&A, 57, 9
Berkhuijsen, E. M., & Wielebinski, R. 1974, A&A, 34, 173
Berkhuijsen, E. M., & Beck, R. 1990, in Galactic and Intergalactic Magnetic Fields, ed. R. Beck, P. P. Kronberg, & R. Wielebinski (Dordrecht: Kluwer), IAU Symp., 140, 201
Berkhuijsen, E. M., Wielebinski, R., & Beck, R. 1983, A&A, 117, 141
Berkhuijsen, E. M., Beck, R., & Gräve, R. 1987, in Interstellar Magnetic Fields, ed. R. Beck, & R. Gräve (Berlin: Springer), 38
Berkhuijsen, E. M., Nieten, Ch., & Haas, M. 2000, in The Interstellar Medium in M 31 and M 33, Proc. 232. WE-Heraeus Seminar, ed. E. M. Berkhuijsen, R. Beck, & R. A. M. Walterbos (Aachen: Shaker), 187
Braun, R. 1990, ApJS, 72, 755
Braun, R. 1991, ApJ, 372, 54
Brinks, E., & Shane, W. W. 1984, A&AS, 55, 179
Burn, B. J. 1966, MNRAS, 133, 67
de Vaucouleurs, G., & de Vaucouleurs, A. 1964, Ref. Catalogue of Bright Galaxies (Austin: Univ. of Texas Press)
Devereux, N. A., Price, R., Wells, L. A., & Duric, N. 1994, AJ, 108, 1664
Emerson, D. T. 1974, MNRAS, 169, 607
Emerson, D. T., & Gräve, R. 1988, A&A, 190, 353
Fletcher, A., Beck, R., Berkhuijsen, E. M., & Shukurov, A. 2000, in The Interstellar Medium in M 31 and M 33, Proc. 232. WE-Heraeus Seminar, ed. E. M. Berkhuijsen, R. Beck, & R. A. M. Walterbos (Aachen: Shaker), 201
Fletcher, A., Beck, R., Berkhuijsen, E. M., & Shukurov, A. 2003, in preparation
Golla, G. 1989, Diploma Thesis, University of Bonn
Guélin, M., Nieten, C., Neininger, N., et al. 2000, in The Interstellar Medium in M 31 and M 33, Proc. 232. WE-Heraeus Seminar, ed. E. M. Berkhuijsen, R. Beck, & R. A. M. Walterbos (Aachen: Shaker), 15
Haas, M., Lemke, D., Stickel, M., et al. 1998, A&A, 338, L33
Han, J. L., Beck, R., & Berkhuijsen, E. M. 1998, A&A, 335, 1117
Heiles, C. 1976, ARA&A, 14, 1
Horellou, C., Beck, R., Berkhuijsen, E. M., Krause, M., & Klein, U. 1992, A&A, 265, 417
Klein, U., Wielebinski, R., & Beck, R. 1984, A&A, 135, 213
Koper, E., Dame, T. M., Israel, F. P., & Thaddeus, P. 1991, ApJ, 383, L11
Nieten, C., Neininger, N., Guélin, M., et al. 2000, in The Interstellar Medium in M 31 and M 33, Proc. 232. WE-Heraeus Seminar, ed. E. M. Berkhuijsen, R. Beck, & R. A. M. Walterbos (Aachen: Shaker), 187
Pooley, G. G. 1969, MNRAS, 144, 101
Ruzmaikin, A., Sokoloff, D. D., Shukurov, A., & Beck, R. 1990, A&A, 230, 284
Sokoloff, D. D., Bykov, A. A., Shukurov, A., Berkhuijsen, E. M., Beck, R., & Poezd, A. D. 1998, MNRAS, 299, 189
Stanek, K. Z., & Garnavich, P. M. 1998, ApJ, 503, L131
Urbanik, M., Otmianowska-Mazur, K., & Beck, R. 1994, A&A, 287, 410
Walterbos, R. A. M. 2000, in The Interstellar Medium in M 31 and M 33, Proc. 232. WE-Heraeus Seminar, ed. E. M. Berkhuijsen, R. Beck, & R. A. M. Walterbos (Aachen: Shaker), 99
Walterbos, R. A. M., & Braun, R. 1994, ApJ, 431, 156
Walterbos, R. A. M., & Gräve, R. 1985, A&A, 150, L1
Walterbos, R. A. M., & Schwering, P. B. W. 1987, A&A, 180, 27
Walterbos, R. A. M., Brinks, E., & Shane, W. W. 1985, A&AS, 61, 451
Wardle, J. F. C., & Kronberg, P. P. 1974, ApJ, 194, 249